Estimation of secondary organic aerosol formation parameters for the Volatility Basis Set combining thermodenuder, isothermal dilution and yield measurements

Petro Uruci[1,2], Dontavious Sippial[3], Anthoula Drosatou[1,2], and Spyros N. Pandis[1,2]

[1]Institute of Chemical Engineering Sciences (FORTH/ICE-HT), 26504, Patras, Greece
[2]Department of Chemical Engineering, University of Patras, 26500, Patras, Greece
[3]Department of Chemical Engineering, Carnegie Mellon University, Pittsburgh, USA

Abstract

Secondary organic aerosol (SOA) is a major fraction of the total organic aerosol (OA) in the atmosphere. SOA is formed by the partitioning onto pre-existent particles of low vapor pressure products of the oxidation of volatile, intermediate volatility, and semivolatile organic compounds. Oxidation of the precursor molecules results in a myriad of organic products making the detailed analysis of smog chamber experiments difficult and the incorporation of the corresponding results into chemical transport models (CTMs) challenging. The volatility basis set (VBS) is a framework that has been designed to help bridge the gap between laboratory measurements and CTMs. The parametrization of SOA formation for the VBS has been traditionally based on fitting yield measurements of smog chamber experiments. To reduce the uncertainty of this approach, we developed an algorithm to estimate the SOA product volatility distribution, effective vaporization enthalpy, and effective accommodation coefficient combining SOA yield measurements with thermograms (from thermodenuders) and areograms (from isothermal dilution chambers) from different experiments and laboratories. The algorithm is evaluated with "pseudo-data" produced from the simulation of the corresponding processes assuming SOA with known properties and introducing experimental error. One of the novel features of our approach is that the proposed algorithm estimates the uncertainty of the predicted yields for different atmospheric conditions (temperature, SOA concentration levels, etc.). The uncertainty of these predicted yields is significantly smaller than that of the estimated volatility distributions for all conditions tested.

1. Introduction

Submicrometer atmospheric particles are of great importance due to their negative effects on public health (Pope and Dockery, 2006; Lim et al., 2012) and their uncertain

influence on Earth's climate (IPCC, 2021). Organic aerosol (OA) contributes 20–90 % to the submicron particulate mass (Zhang et al., 2007) and is emitted directly in the atmosphere as primary particles (POA) or formed as secondary organic aerosol (SOA). SOA constitutes a major fraction of the total OA in the atmosphere contributing more than 60 % on average (Kanakidou et al., 2005). SOA is formed by the condensation of low vapor pressure products of the oxidation of volatile (VOCs), intermediate volatility (IVOCs), and semi-volatile organic compounds (SVOCs).

Hundreds of mostly unknown products are formed during the oxidation of each SOA precursor making the detailed description of the corresponding reactions and eventual SOA formation extremely challenging. The volatility basis set (VBS) is one approach that has been proposed to simplify the system and to allow the SOA simulation in CTMs. The VBS describes the volatility distribution of OA using a set of surrogate species with effective saturation concentrations that vary by one order of magnitude (Donahue et al., 2006; Stanier et al., 2008). Volatility is one of the most important physical properties of SOA components as it determines to a large extent their gas-particle partitioning (Pankow, 1994a; 1994b). The parametrization of SOA formation for the VBS requires the determination of the yields of each volatility bin (volatility distribution of products) and the corresponding enthalpies of vaporization.

The SOA parametrizations for the VBS have been traditionally based on fitting yield measurements (Lane et al., 2008). The major weakness of this approach is that the resulting parametrization is limited to the range of OA concentrations and temperatures of the measurements. In most cases, the concentration range does not include the low concentrations relevant to the atmosphere and usually most of the experiments take place in a relatively narrow temperature range. Pathak et al. (2007a) needed 37 smog chamber experiments at different temperatures (0–45 $^{\circ}$C) and atmospherically relevant concentrations to constrain the α-pinene SOA temperature sensitivity.

A number of approaches has been used to minimize the number of experiments needed to characterize the temperature dependence of the SOA formation. Stanier et al. (2007) developed an experimental technique with which the temperature-controlled smog chamber could be heated or cooled after the SOA formation moving the system to new equilibrium favoring evaporation or condensation respectively. However, interactions of the SOA with the walls of the system increased the uncertainties of the approach. Stanier et al. (2008) presented an algorithm to fit the smog chamber

experiments using several volatility bins. However, the number of experiments needed by the algorithm should cover a wide range of concentrations and temperatures to effectively constrain the stoichiometric mass yields and the effective vaporization enthalpy.

In an effort to cover a wider concentration and temperature range, thermodenuder measurements can be used. The thermodenuder (TD) is a common instrument developed to characterize the volatility of atmospheric aerosols by heating them and observing the resulting changes in size, mass, optical properties, etc. (Burtscher et al., 2001; Wehner et al., 2002, 2004; An et al., 2007). TDs consist of a heated tube in which the volatile particle components evaporate followed by a cooling section with activated carbon to avoid vapor recondensation. The mass changes in TDs depend on the initial SOA concentration, the residence time in the heating tube, the vaporization enthalpy, and the mass transfer resistances. The latter are described by the effective accommodation coefficient that has been traditionally used to account for resistances to mass transfer not only at the surface of the particle but also inside the particle. The evaporation rate for most particles is relatively insensitive to its value when this value is around one. A typical way of reporting the TD measurements is by calculating the aerosol mass fraction remaining (MFR) at a given temperature after passing through the TD. The MFRs in a range of TD temperatures constitute the thermogram.

In applications in the field (Cappa and Jimenez, 2010; Huffman et al., 2009; Lee et al., 2010; Louvaris et al., 2017a) and in the laboratory (Kalberer et al., 2004; Baltensperger et al., 2005; An et al., 2007; Lee et al., 2011; Cain et al., 2020) the particles do not reach equilibrium with the gas phase inside the TD. Therefore, dynamic aerosol evaporation models (Riipinen et al., 2010; Cappa, 2010; Fuentes and McFiggans, 2012) are needed for the interpretation of TD measurements. Karnezi et al. (2014) used the time-dependent evaporation model of Riipinen et al. (2010) to calculate the OA volatility distribution, vaporization enthalpy, and mass accommodation coefficient from TD measurements. The authors showed that a simple error minimization approach may not be appropriate for such systems as very similar thermograms can be obtained for multiple combinations of different parameters. For this reason, their approach estimates an ensemble of "good" solutions, from which the best estimate and the corresponding uncertainties are derived.

Grieshop et al. (2009) suggested the combination of TD and isothermal dilution to constrain the volatility distribution of SOA. Karnezi et al. (2014) proposed an algorithm to include both types of measurements. The authors concluded that the combination of the two types of measurements can better constrain the OA volatility than each set separately. Louvaris et al. (2017b) and Cain et al. (2020) applied this algorithm to cooking OA (COA) and SOA, respectively. Louvaris et al. (2017b) showed that the use of only TD measurements led to overestimation of the SVOC fraction of COA, while the use of TD and isothermal dilution data reduces the uncertainty of the volatility distribution and the effective vaporization enthalpy. Cain et al. (2020) conducted TD and isothermal dilution experiments for α-pinene and cyclohexene ozonolysis SOA. The SOA in these two systems had similar thermograms, but different areograms. When only thermograms were used in the model, the volatility distributions were quite similar. However, the addition of areograms revealed that α-pinene ozonolysis SOA consists mostly of low-volatility organic compounds (LVOCs) and the cyclohexene ozonolysis SOA consists mostly of SVOCs.

To constrain the volatility product distribution of SOA and its effective vaporization enthalpy, we combine TD and isothermal dilution experiments with the SOA yield measurements. We extend here the algorithm of Karnezi et al. (2014) by introducing additional inputs (SOA yields) and by providing additional outputs (uncertainty of estimated yields in relevant atmospheric conditions). The algorithm is tested with "pseudo-experimental" data generated from the use of models simulating the corresponding measurement processes, therefore the true parameters are known. The results of the "pseudo-experiments" are corrupted so that they include experimental errors.

2. Model Description

2.1. SOA Formation

Gas-phase oxidation of VOCs involves a large number of reactions and produces a large number of products that can condense in the particulate phase. Depending on their effective saturation concentration, they can be represented in the 1D-VBS framework by

$$VOC + oxidant \rightarrow \alpha_1 P_1 + \alpha_2 P_2 + ... + \alpha_n P_n + \text{volatile products} \qquad (1)$$
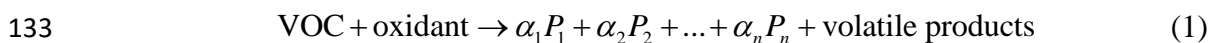
134 where n is the number of the surrogate compounds (volatility bins in the VBS), P_i is the

135 surrogate product in the i-th volatility bin and α_i is the corresponding stoichiometric

136 mass yield. The total SOA mass yield can be then calculated as:

$$137 \quad Y \equiv \frac{C_{\mathrm{OA}}}{\Delta \mathrm{VOC}} = \sum_i^n \frac{\alpha_i}{1 + \left(C_i^*/C_{\mathrm{OA}}\right)} \qquad (2)$$

138 where C_{OA} is the total SOA concentration, $\Delta \mathrm{VOC}$ is the consumed concentration of the

139 VOC and C_i^* is the effective saturation concentration of compound i. This yield

140 equation is an extension of the two-product model by Odum et al. (1996) replacing their

141 semi-empirical partitioning coefficients with the assumption of a pseudo-ideal solution

142 (Strader et al., 1999). This model assumes that the system has reached equilibrium when

143 the yield was measured and that the differences in molecular weights are small.

144 The effective saturation concentrations at different temperatures are given by

145 the Clausius-Clapeyron equation:

$$146 \quad C_i^*(T) = C_i^*(T_{\mathrm{ref}}) \frac{T_{\mathrm{ref}}}{T} \exp\left[\frac{\Delta H_{\mathrm{vap},i}}{R}\left(\frac{1}{T_{\mathrm{ref}}} - \frac{1}{T}\right)\right] \qquad (3)$$

147 where T_{ref} is the reference temperature in which the reference effective saturation

148 concentration is defined (298 K in this work), and $\Delta H_{\mathrm{vap},i}$ is the enthalpy of vaporization

149 of surrogate compound i.

150

151 2.2. Thermodenuder Model

152 The time-dependent evaporation of SOA in the TD used in this work is described by

153 the dynamic mass transfer model of Riipinen et al. (2010). The evolution of the total

154 particle mass, m_{p}, and the gas phase concentration of the compound i, C_i are given by:

$$155 \quad \frac{dm_{\mathrm{p}}}{dt} = -\sum_{i=1}^n I_i \qquad (4)$$

$$156 \quad \frac{dC_i}{dt} = I_i N_{\mathrm{tot}} \qquad (5)$$

157 where n is the number of surrogate compounds, N_{tot} is the total number concentration

158 of particles (assuming monodisperse aerosol population) and I_i is the mass flux of

159 compound i from the gas to the particulate phase for each particle calculated by

160 (Seinfeld and Pandis, 2016):

$$161 \quad I_i = \frac{2\pi d_{\mathrm{p}} M_i \beta_{\mathrm{m}i} D_i}{R T_{\mathrm{TD}}}\left(p_i - p_i^0\right) \qquad (6)$$

where d_p is the particle diameter, R is the ideal gas constant, M_i is the molecular weight of compound i, D_i is the diffusion coefficient of compound i in the gas phase at temperature T_{TD}, p_i and p_i^0 are the partial vapor pressures of i far away from the particle and at particle surface, respectively, and β_{mi} is a factor for the correction of kinetic and transition regime effects (Fuchs and Sutugin, 1970):

$$\beta_{mi} = \frac{1 + Kn_i}{1 + \left(\dfrac{4}{3\alpha_{mi}} + 0.377 \right) Kn_i + \dfrac{4}{3\alpha_{mi}} Kn_i} \tag{7}$$

where Kn_i is the Knudsen number of compound i, and α_{mi} is the mass accommodation coefficient of compound i on the particles. The partial vapor pressure of compound i at the particle surface is given by:

$$p_i^0 = x_{mi} \frac{C_i^* RT}{M_i} \exp\left(\frac{4 M_i \sigma}{R T_{TD} \rho d_p} \right) \tag{8}$$

where x_{mi} is the mass fraction of compound i in the particulate phase, C_i^* is the effective saturation concentration, σ is the surface tension (assumed 0.05 N m^{-1} in our simulations), T_{TD} is the particle temperature assumed to be the same as in the TD, and ρ is the particle density. The effective saturation concentrations at different TD temperatures are given by Eq. (3).

Processes other than organic aerosol evaporation may affect the TD measurements. For example, thermal decomposition may accelerate the transfer of organic compounds from the particulate to the gas phase and may lead to overestimation of the volatility of especially the least volatile components of the SOA (Epstein et al., 2010; Saha and Grieshop, 2016; Stark et al., 2017). However, the corresponding parameters for the SVOCs and the more volatile LVOCs that are important for atmospheric SOA modeling should be a lot less uncertain given that they are measured in relatively low TD temperatures. The use of isothermal dilution measurements may also help identify cases in which the model does not include a process (e.g., thermal decomposition) that dominates the behavior of the aerosol during heating. In this case, one expects that the overall algorithm will have difficulties reproducing all measurements (yields, isothermal dilution, and evaporation in the TD).

2.3. Isothermal Dilution Model

In isothermal dilution experiments, a SOA sample is injected in a reactor filled with clean air at room temperature. The concentrations of both the gas and particulate phase components are lowered due to dilution leading the system out of equilibrium. The evaporation of SOA as a result of isothermal dilution is also described by equations (3)-(8) (Karnezi et al., 2014), but the temperature is equal to 298 K. Evaporation in a dilution chamber depends on the initial SOA mass, time, and the α_m, but not on ΔH_{vap} as the particles evaporate without a change in temperature.

The dilution ratio is an important parameter, varying typically from 10 to 20 in SOA experiments (Cain et al., 2020). Low dilution ratios result in little evaporation and little signal to be explored by the parameter estimation algorithm. High dilution ratios lead to very low initial concentrations in the dilution chamber and a lot of noise in the subsequent evaporation measurements.

3. Algorithm for the Estimation of VBS Parameters

The algorithm of Karnezi et al. (2014) was first extended to include an SOA partitioning model described by Equations (1) – (3) together with the TD and isothermal dilution models in order to estimate the volatility product distribution, vaporization enthalpy and accommodation coefficient. We discretized the domain of the parameters and simulated all combinations of stoichiometric mass yields (α_i), ΔH_{vap}, and α_m. The yields α_i were allowed to vary from 0.0 to 0.8, with values of 0.0, 0.05, 0.1, 0.15, 0.2, 0.3, 0.4, 0.6, and 0.8. The user of the algorithm can specify an upper limit for the sum of the yields to reduce the number of the potential solutions that the algorithm will test. Combinations with sum of the yields exceeding 1.0 were excluded from the analysis originally. The sensitivity of our results to setting the upper limit of the sum of the yields equal to 2 is examined in Section 4.6. For a 4-product system there are 3,153 and for 6-product system 66,636 acceptable combinations. The values used for ΔH_{vap} were from 20 to 200 kJ mol^{-1} with a step of 20, and for α_m, the values used were 0.001, 0.01, 0.1, and 1. As a result 126,120 simulations are needed (computational time of about 15 h in an office PC) for a 4-product VBS and 2,665,440 for a 6-product solution.

For each simulation and each type of measurement, we calculated the *normalized mean square error* (NMSE) defined as

$$\text{NMSE} = \frac{\sum\limits_{i=1}^{N_O}\left(P_i - O_i\right)^2}{\sum\limits_{i=1}^{N_O} O_i} \tag{9}$$

222

where O_i represents the ith observed value (corresponding to a specific SOA concentration for yield measurements or temperature for TD, or time for isothermal dilution), P_i the corresponding model-predicted value, and N_O is the total number of observations from each type of measurement. For each simulation (denoted as s), the overall error was calculated by assuming equal weight to the set of yield, TD, and dilution measurements and summing the corresponding errors:

229
$$E_s = \text{NMSE}_{Y,s} + \text{NMSE}_{\text{TD},s} + \text{NMSE}_{\text{Dil},s} \tag{10}$$

The parameter combinations for which the overall error E_s is less than 5% are identified. The best solution is then calculated by averaging these solutions using the inverse error E_s as a weighting factor. The solutions that are closer to the measurements have higher weight. Therefore, for every combination of α_i, ΔH_{vap}, and α_m the algorithm calculates one overall *NMSE* following Eq. (10) and all data points for each solution get the same weighting factor. More specifically the best estimate $\bar{x}$ is given by:

236
$$\bar{x} = \frac{\sum\limits_{k}^{N} x_k \dfrac{1}{E_k}}{\sum\limits_{k}^{N} \dfrac{1}{E_k}} \tag{11}$$

where x_k is the estimated value of a property (mass yield of a volatility bin, effective vaporization enthalpy, or effective accommodation coefficient) and N is the number of combinations with error below the threshold value. The uncertainty range of the parameters is estimated by calculating the standard deviation (σ):

241
$$\sigma = \sqrt{\frac{\sum\limits_{k}^{N}\left[\left(x_k - \bar{x}\right)^2 \cdot \dfrac{1}{E_k}\right]}{\sum\limits_{k}^{N} \dfrac{1}{E_k}}} \tag{12}$$

242 following Karnezi et al. (2014).

243

4. Testing of the Algorithm

4.1. Generation of Data for Evaluation

In order to evaluate the algorithm, we generated data using the output of SOA formation, thermodenuder and isothermal dilution models described in Section 2 for systems with known volatility distribution of the products, and properties. Then, these data were "corrupted" with random errors to represent the "noise" observed in laboratory measurements for yields, thermograms, and areograms. As a result, there is no set of model parameters that can reproduce all the "measurements". The yields were corrupted based on the variability of laboratory measurements of Pathak et al. (2007a), by assuming a normal distribution and standard deviation (σ_Y) given by:

$$\sigma_Y = 0.1\,Y_{\text{true}} + 0.02 \tag{13}$$

where Y_{true} are the correct yields.

For TD, the errors were calculated by assuming a normal distribution and the standard deviation (σ_{TD}) suggested by Karnezi et al. (2014):

$$\sigma_{\text{TD}} = 0.51\,MFR_{\text{TD,true}} - 0.5\left(MFR_{\text{TD,true}}\right)^2 \tag{14}$$

where $MFR_{\text{TD,true}}$ are the correct MFR values for each TD temperature.

For dilution, the errors were calculated by assuming a uniform distribution and standard deviation (σ_{Dil}) suggested by Karnezi et al. (2014):

$$\sigma_{\text{Dil}} = 0.05\,MFR_{\text{Dil,true}} + 0.03 \tag{15}$$

where $MFR_{\text{Dil,true}}$ are the correct MFR values for isothermal dilution.

Based on the above methodology, we generated "pseudo-measurements" of yield, TD, and isothermal dilution for different SOA systems. The parameters used to produce the pseudo-experimental data are summarized in Table S1. The "experimental" conditions assumed for the TD and isothermal dilution measurements are shown in Table S2.

In "Experiment" A, we test the performance of the algorithm against α-pinene ozonolysis data and examine the effect of TD and isothermal dilution data. For "Experiment" A, the "true" values were taken from the parameterization derived by Pathak et al. (2007b) for the ozonolysis of α-pinene at low NO_x, dark and low RH conditions. Therefore, these results are good fits of the measurements analyzed in that study. The parametrization was derived assuming a 4-volatility bin system with saturation concentrations ranging from 1 to 10^3 μg m^{-3}. The effective vaporization enthalpy estimated in that study was equal to 30 kJ mol^{-1}. Because the effective

accommodation coefficient was not part of the Pathak et al. (2007b) parametrization, we assumed a value of 0.5 in this work. We used a small number of yield measurements at atmospherically relevant SOA concentrations of 1, 5, 10, 20 and 40 μg m^{-3} (Fig. 1). For this SOA system, the yield at 40 μg m^{-3} did not exceed 20%. The thermogram includes ten MFR data points in the temperature range of 20 to 200 ^{o}C. For the highest temperature, more than 70% of the SOA mass was evaporated. The areogram shows that the correspondent SOA evaporated almost by 70 % in the first 0.5 h and more than 90% in less than 3 h.

For "Experiment" B, the "true" values were taken from the alternative parametrization proposed by Pathak et al. (2007b) for the same oxidation system as described before. This time, the authors used a 7-volatility bin system with saturation concentrations ranging from 10^{-2} to 10^4 μg m^{-3} in their parametrization. The effective vaporization enthalpy of the parametrization was 30 kJ mol^{-1}, while for the accommodation coefficient we assumed again a value of 0.5. The yield, TD and isothermal dilution "measurements" of Experiment B are generated in the same SOA mass concentration, temperature, and dilution time range as in the previous pseudo-experiment (Fig. 2).

For "Experiment" C, the "true" values were based on the parameterization of the SOA formed during α-humulene ozonolysis by Sippial et al. (2022). The authors measured high SOA yields for α-humulene in the main smog chamber (~70% at 60 μg m^{-3}), and their corresponding thermogram suggested that the SOA particles fully evaporated at 150 ^{o}C, while the areogram showed modest (20%) evaporation in the dilution chamber after 3 hours. A 4-volatility bin set with saturation concentrations ranging from 10^{-2} to 10 μg m^{-3} was used in that study to fit the measurements. The stoichiometric coefficients of the three least volatile bins (10^{-2}, 10^{-1} and 1 μg m^{-3}) were around 0.1 and for the most volatile (10 μg m^{-3}) 0.25. The vaporization enthalpy was 115 kJ mol^{-1} and the accommodation coefficient was 0.01 (Table S1). We assumed five yield "measurements" in the SOA concentration range of 1 to 100 μg m^{-3} with yield values as high as 65 % at 100 μg m^{-3} (Fig. 3). The corresponding thermogram consisted of 10 data and the particles fully evaporated at TD temperatures higher than 150 ^{o}C. The areogram consisted of 17 data points and only 20 % of the SOA evaporated in the dilution chamber.

4.2. Parameter Estimation for "Experiments" A, B, and C

We explored the performance of the algorithm for different choices of the number of volatility bins, the range of saturation concentrations, and the range of SOA mass concentration range in the yield measurements. For each test, the "true" and the estimated properties are summarized in Table 1.

We evaluated the performance of our parameter estimation algorithm comparing its predictions both against the "measurements" and the "truth" defined as the predictions of the original parameterization. In both comparisons, *mean normalized error* (MNE) (Emery et al., 2017) was used as the evaluation metric because it has a simpler physical meaning than NMSE.

For the evaluation against the "measurements", the MNE_M was defined as

$$MNE_{\mathrm{M}} = \frac{100}{N_O} \sum_{i=1}^{N_o} \frac{\left| EST_i - O_i \right|}{O_i} \tag{16}$$

where EST_i is the estimated by the algorithm value and corresponds to a specific measured point O_i.

For the evaluation against the "truth", which includes conditions (e.g., temperatures or concentrations) for which there are no available measurements, the MNE_T was defined as:

$$MNE_{\mathrm{T}} = \frac{100}{N_d} \sum_{j=1}^{N_d} \frac{\left| EST_j - TR_j \right|}{TR_j} \tag{17}$$

where EST and TR are the estimated and the "true" values respectively. N_d is the total number of data points included in calculations and depends on the selected discretization of the corresponding dependent variable (e.g., SOA concentration, TD temperature, and dilution time). We used a linear discretization for the SOA concentrations (from 0.01 to 50 μg m^{-3} with a step of 0.01) and the TD temperatures (20 to 200 °C with a step of 5 °C but excluding zero MFR values to avoid the division by zero). For the dilution time, the sampling time step was not constant. We used a higher resolution for the first 0.5 hour (step of 2 min), in which the evaporation is usually faster, and a lower resolution afterwards (step of 10 min).

Finally, we used the average relative standard deviation (*ARSD*) as a metric to quantify the uncertainty of the estimates (range of good solutions) using the same discretization as in the MNE_T metric. The *ARSD* is given by:

$$ARSD = \frac{100}{N_d} \sum_{j=1}^{N_d} \frac{\sigma_j}{EST_j} \qquad (18)$$

where σ_j is the standard deviation for data point j.

4.2.1 Parameter Estimation for "Experiment" A

In Test A1, we applied the algorithm in the same range of saturation concentrations and with the same number of volatility bins as these used to produce the "experimental" data. The upper bin (10^3 µg m^{-3}) exceeded the maximum SOA concentration (40 µg m^{-3}) in the measurement range by one order of magnitude.

Figure 1 depicts the estimated and the range of the ensemble of best solutions for the three types of "measurements" for Test A1. There were 148 "good" solutions under the 5% threshold out of the 126,120 simulations (Table S3). The density distribution of the solutions is depicted in Figure S1. The performance of the model for the yields at 25 ^{o}C was quite encouraging with a small tendency of overprediction for SOA higher than 10 µg m^{-3}. The MNE_M of the model for the SOA yield "measurements" (given by Eq. 16) was equal to 25% (Table 2). The corresponding discrepancy between the true parameterization and the measurements (due to the measurement error that we introduced) was 21.2% (Table 2). This indicates that a significant part of the algorithm error can be explained by the uncertainty introduced in the measurements.

Our algorithm can be used to calculate the SOA yield at different concentrations and temperatures. The yields were calculated in the atmospherically relevant range of 0–50 µg m^{-3} SOA concentration and at four temperatures (5, 15, 25, and 35 ^{o}C) using the true parameter values and the estimated parameters of Test A1 (Fig. 1a-d). At 25 ^{o}C (Fig. 1c), the estimated yield curve is in good agreement with the "true" yield curve for SOA concentrations lower than 6 µg m^{-3} (error of 8% at 6 µg m^{-3}), but the discrepancies increase at higher concentrations (error of 23% at 50 µg m^{-3}). The average MNE_T error between the true parametrization and the estimated values (given by Eq. 17) was equal to 17.3% for yields at 25 ^{o}C (Table 3). The uncertainties, as expected, are larger at lower temperatures. However, the MNE_T error (estimated yields compared to the true value) remains less than 25% (Table 3) even at 5 ^{o}C, quite far from the measurement temperature. Both MNE_T and MNE_M were quite close to the introduced experimental error. Their difference can be explained by both the "noise" introduced to the

371 "measurements" that affects MNE_M and the higher number of points used to calculate
372 MNE_T.

373   The SOA model used in this work assumes that the stoichiometric coefficients
374 (α_i) are temperature independent. Therefore, processes, such as formation of highly
375 oxygenated organic molecules (HOMs) and oligomerization which are expected to be
376 temperature dependent (Quéléver et al., 2019; Gao et al., 2022), are not described by
377 our algorithm.

378   The algorithm provides a range of "good" estimates in addition to the best
379 estimate. The range can be defined by the lower and upper SOA yield limits of the
380 ensemble of the good solutions at each point. At 25 °C, the yield range increased, as
381 expected, at higher concentrations (yield range of 0.05 at 1 µg m^{-3} to 0.17 at 50 µg
382 m^{-3}). The average relative standard deviation ($ARSD$ of the estimated yields defined by
383 Eq. 18) was equal to 26% (Table 4) for the 25 °C case. For the rest of the temperatures,
384 the $ARSD$ increased for the lower temperatures, ranging from 24% at 35 °C to 35% at
385 5 °C (Table 4) and including in all cases the true solution.

386   For the TD (Fig. 1e), the model reproduced well the correspondent thermogram
387 with low errors compared to the "measurements" with an error MNE_M of 7% (Table 2).
388 The error MNE_T compared to the "true" values was 5.5% (Table 3). The error of the
389 TD "measurements" compared to the true values was equal to 7.6% (Table 2).
390 Therefore, the error of the proposed algorithm is quite similar to the experimental error.
391 The error introduced into the "measurements" was transferred, as expected, to the error
392 metrics of the algorithm.

393   For the isothermal dilution (Fig. 1f), the algorithm did reasonably well for the
394 first 30 minutes and then the evaporation was slightly underpredicted leading to an error
395 MNE_M of 16.7% (Table 2). This MNE_M value was roughly two times higher than the
396 corresponding error between the dilution measurements and the true parametrization
397 (Table 2). The error between the estimated and the "true" values MNE_T was 19%. The
398 $ARSD$ of 24% (Table 4) was sufficient to include the true solution.

399   The estimated volatility distribution of the products and the effective
400 vaporization enthalpy and accommodation coefficient using the three types of
401 measurements can be seen in Figure 4 and Table 1. The estimated volatility distribution
402 of the products was in a good agreement with the "true" values (α_i absolute difference
403 of 0.01 at 1 µg m^{-3}, 0.03 at 10 µg m^{-3}, 0.07 at 10^2 µg m^{-3}, and 0.04 at 10^3 µg m^{-3}) and
404 the estimated uncertainties contained the correct values. There is a large uncertainty

range for the two higher volatility bins (standard deviation higher than 0.13) indicating that yield values at higher SOA concentrations would be needed to better constrain these volatility bins. The relative error of the estimated ΔH_{vap} is 10%. The estimated accommodation coefficient was 0.17 compared to a true value of 0.5. The estimated uncertainty for the effective accommodation was almost one order of magnitude (from 0.06 to 0.51) indicating the difficulty of constraining this parameter when it is close to unity and thus the resistances to mass transfer are small.

4.2.2 Parameter Estimation for "Experiment" B

In this section, we analyze the pseudo-experimental data of Experiment B, which were obtained from the parametrization of the same smog chamber results used in Experiment A, but with more components and a much wider range of volatilities including LVOCs, SVOCs and IVOCs (10^{-2}–10^4 µg m^{-3}). In Test B1, the algorithm was applied using a 4-bin VBS with saturation concentrations ranging from 1 to 10^3 µg m^{-3}. In this test, we attempted to model the behavior of the system with a narrower volatility range than the real one. The upper limit of the saturation concentration range that we tested did not exceed the 10^3 µg m^{-3} because Experiment B took place in moderate SOA concentration levels (up to 40 µg m^{-3}), which means that it is practically impossible to constrain the 10^4 µg m^{-3} or higher volatile bins. Figure 2 shows the results of the fitting for the three types of "measurements" in this experiment. There were 82 "good" solutions under the 5% threshold out of 126,120 simulations (Table S3) and the density of the solutions are shown in Figure S2. At 25 °C, the model performance for the yields is encouraging (MNE_M=20.6%). This is again pretty close to the measurement error (20.5%). By comparing the estimated and the "true" yield curves at 25 °C, the error MNE_T is now 14%. The error increases to 31% at 5 °C, far from the available measurements. This is reflected also in the increase of the uncertainty of our estimates with the $ARSD$ increasing from 17% at 35 °C to 37% at 5 °C (Table 4). Once more the uncertainty range estimated by the algorithm includes the true values.

Both "measured" and "true" thermogram were well captured by the best estimate (MNE_M of 6% and MNE_T of 4%) with an uncertainty $ARSD$ of 20.5%. The evaporation in the dilution chamber was a little underestimated for the first 2 h, but then it was slightly overpredicted. The MNE_T for the areogram was 13.3% and the true values were included within the range of the estimates ($ARSD$ of 18%).

438   Figure 5 shows the results of Test B1 for the volatility distribution of the
439   products. The "true" stoichiometric coefficient for the 1 μg m^{-3} bin was overestimated
440   by 0.01 by the algorithm. This overestimation actually corresponds to the total material
441   of the 10^{-2} and 10^{-1} μg m^{-3} bins of the "true" system. This indicates that the algorithm
442   places the material of the two lowest bins that are not part of the solution to the bin with
443   the lower volatility. For the 10 μg m^{-3} and 10^2 μg m^{-3} bins, the relative errors between
444   the estimated and "true" were 58% and 277% respectively (Table S4), while for the 10^3
445   μg m^{-3} bin, the relative error was 10 %. The ΔH_{vap} was predicted accurately (error of
446   only 4%), while α_m was underpredicted (0.1 instead of 0.5). The model compensates
447   for the missing volatility bins by increasing the material in the 10^2 μg m^{-3} bin and by
448   decreasing the accommodation coefficient.

449   The results of Test B1 suggest that the mismatch between the actual SOA
450   volatility distribution and the range used for the fits can introduce significant errors in
451   the retrieved distribution for individual volatility bins. However, despite these
452   problems, the yields predicted by the derived parameterizations have a much lower
453   error than the volatility distribution. This is a valuable insight for the strengths and
454   weaknesses of this and other similar SOA parameter estimation algorithms.

455

456   **4.2.3 Parameter Estimation for "Experiment" C**
457   In Test C1, we obtained the best fits for the pseudo-measurements of Experiment C by
458   applying the algorithm in the same range of saturation concentrations and with the same
459   number of volatility bins (4 volatility bins in the 10^{-2}–10^1 μg m^{-3} saturation
460   concentration range) as the true volatility distribution.

461   Figure 3 shows the results of the fitting for the three types of "measurements".
462   There were 3,479 "good" solutions under the 5% threshold out of the 126,120
463   simulations (Table S3). The density distribution of the solutions is shown in Figure S3.
464   The best estimate for the SOA yields at 25 ^{o}C was in a good agreement with the
465   "measurements" (MNE_M=6.3%) and the "true" values (MNE_T=9.6%). For the rest of
466   the temperatures, there was a decreasing trend of the error as the temperature decreased
467   varying from 15.5% at 35 ^{o}C to 6.2% at 5 ^{o}C. A similar decreasing trend was observed
468   for the uncertainty $ARSD$ of the estimates which varied from 23% at 35 ^{o}C to 15% at 5
469   ^{o}C. This behavior is the opposite from what we observed in the previous tests, in which
470   both errors and uncertainties increased at lower temperatures. However, the changes in
471   both the error and the uncertainty are small (change of around 7% between the upper

and lower temperature for both metrics), indicating that this system is less temperature-sensitive in this temperature range than the previous ones.

The performance of the algorithm was satisfactory compared to the TD "measurements" (MNE_M=12.9%). The corresponding error of the algorithm for the true values (MNE_T) was 4.4% for temperatures up to 110 ^{o}C and equal to 10.6% for the lower values at higher temperatures. According to Figure 3, the evaporation due to dilution was initially overestimated for the first 30 min, but then underestimated (highest MFR discrepancy of 0.05) and there is a high uncertainty range of the corresponding estimates (MFR range of 0.46 at 3 h). However, the low dilution values resulted in low relative errors (MNE_M of 3.5% and MNE_T of 2.7%).

Figure 6 shows that the highest relative errors were calculated for the 10^{-1} and 10^0 μg m^{-3} bins (23% and 33% respectively), and smaller relative errors for the other two bins (less than 13%). The uncertainties were almost of the same magnitude for all bins with standard deviations ranging from 0.09 to 0.13. The performance of the model was good for the ΔH_{vap} (relative error of 7%), but with high uncertainty for α_m.

4.3. Effect of the Volatility Range

In in this section, we explore the performance of the algorithm for different choices of the number of volatility bins and the range of saturation concentrations. The analysis of the results of Test B1 has already quantified the effects of using a narrower volatility distribution in the parameter estimation algorithm than the one of the investigated SOA system. Additional sensitivity tests are performed here for all cases.

In Test A2, we used 3 volatility bins covering the $1–10^2$ μg m^{-3} saturation concentration range instead of the 4 bins used in Test A1. The narrower assumed volatility range had a very small effect on the estimated yields at all temperatures (Table 3 and Fig. S4) compared to Test A1. The change in MNE_T ranged from 3% at 5 ^{o}C to 0.3% at 35 ^{o}C. Minor changes were detected in the predicted thermogram (change of 0.8%) and areogram (change of 0.5%) as well. The uncertainty of the yield estimates increased by less than 2.5% at all temperatures. The estimated volatility distribution of the SOA products of Test A2 changed by less than 5% in the two lower bins. The material in the 10^2 μg m^{-3} increased by 15% to account for the SOA of higher volatility that could not be included otherwise in the estimated distribution. The estimated ΔH_{vap} was in this case 32 kJ mol^{-1} (2.7% decrease) and the α_m decreased by 12% with respect to Test A1.

506   In Test A3, we shifted the assumed 4-bin volatility distribution by one order of

507   magnitude to lower values (from 1–1000 μg m^{-3} in Test A1 to 0.1–100 μg m^{-3} in Test

508   A3). In this case, the algorithm distributed exactly the same material to the 1, 10 and

509   100 μg m^{-3} volatility bins as in Test A2, and it predicted correctly zero SOA in the 0.1

510   μg m^{-3} bin (Table 1). The ΔH_{vap} and α_m estimated values were also unchanged with

511   respect to Test A2. This in turn, led to the same estimated yields at different

512   temperatures (no change in the error between the two tests).

513   In Test C2, we applied the algorithm against the Experiment C "measurements"

514   using a 4-volatility bin system in the 1 to 10^3 μg m^{-3} range, that is two orders of

515   magnitude higher than the actual range of the "true" values. Figure 7 shows the results

516   of the fitting for the three types of "measurements". Despite the significant mismatch

517   of the volatility distributions the MNE_M increased by only 2.3% for the estimated SOA

518   yields. The error for the TD measurements increased by 20% while it actually decreased

519   a little (1.2%) for the dilution data. The errors compared to the true values increased by

520   less than 3% for the temperature range 15–35 °C while it increased by 12% at 5 °C.

521   These results suggest that the estimated yields are quite robust in this case to the

522   assumed volatility range. The major effect of the mismatch in volatility ranges was

523   evident in the predicted thermogram with overestimation of the MFR for the 60–120

524   °C temperature range and underprediction in higher temperatures. The increase in

525   MNE_T for the TD MFR was 17.2% (Table 3). The change in the predicted areogram

526   was marginal and led to a small increase of MNE_T (error increase by 0.7%) (Table 3).

527   The algorithm underestimated again the α_m (0.004 instead of 0.01) but also recognized

528   the high uncertainty of the corresponding estimate. The algorithm distributed

529   significant material to the 1 μg m^{-3} bin (3.6 times higher than the actual), in an effort to

530   account for the absence of the 10^{-2} and 10^{-1} μg m^{-3} bins. The ΔH_{vap} was underestimated

531   with an error of 21%.

532   The results of the above tests indicate that a mismatch between the true and

533   assumed volatility ranges of the SOA increases in general the estimation error but the

534   increase is small to modest. This is reassuring for the robustness of the proposed

535   algorithm.

536

537   **4.4. Effect of Measurements at High SOA Levels**

538   During the last decade there has been a significant shift of the performed SOA smog

539   chamber towards lower SOA concentrations. This is needed to increase the accuracy at

540 the ambient concentration levels. The high SOA concentration experiments that once

541 represented the majority of the performed experiments are becoming increasingly rare.

542 In this paragraph we examine the value of these high concentration experiments for the

543 estimation of SOA yields at ambient conditions.

544   To examine the effect of "measurements" at SOA levels much higher than the

545 atmospheric ones, we included an extra yield measurement at 200 μg m^{-3} in the yield

546 data of Experiments A and B. In Test A4 and B2, we applied the algorithm once again

547 against the three types of "measurements" by using a 4-volatility bin system with

548 saturation concentrations ranging from 1 to 10^3 μg m^{-3}.

549   In Test A4, the additional experiment at high SOA concentration led to an MNE_T

550 of 15.7% for the yields at 25 ^{o}C (Table 3 and Fig. S5), which is by 1.6% lower than that

551 without this experiment in Test A1. The improvement was more significant at lower

552 temperatures e.g., the MNE_T at 5 ^{o}C was reduced from 24.4% to 20.4%. The reduction

553 in the $ARSD$ for the SOA yields ranged from 3.8% at 5 ^{o}C to 0.9% at 35 ^{o}C (Table 4).

554 Figure 8 depicts the results of the model for the yields and the volatility distribution of

555 the products for Test A4. The accuracy of the predicted volatility distribution increased

556 especially for the higher volatility material. For example, the error for the 10^2 μg m^{-3}

557 bin was reduced from 41% in Test A1 to 6% in this case (Table S3). Minor changes in

558 the errors were detected for the ΔH_{vap} and α_m between the two tests (3% increase and

559 6% decrease respectively).

560   Similar to Test A4, in Test B2 we added a yield measurement at 200 μg m^{-3} in

561 the Experiment B set of "measurements". Figure 9 depicts the results of the model for

562 the SOA yields at 25 ^{o}C and the estimated volatility distribution of the products. The

563 use of the additional data point led to a reduction of the NME_T from 13.9% in Test B1

564 to 9% in Test B2 at 25 ^{o}C (Table 3). Similar reductions in the NME_T were observed for

565 the other temperatures, with the highest one observed at 5 ^{o}C (lower error by 7%)

566 (Figure 10). The reduction in the $ARSD$ for the estimated yields ranged from 3.3% at 5

567 ^{o}C to 1.2% at 35 ^{o}C (Table 4). Minor changes were observed for the estimated

568 thermogram (Fig. S6) (change in the NME_T of 1.5%) and the uncertainty of the

569 estimates (change in the $ARSD$ of 2.5%). The error in the estimated areogram was also

570 small but in this case the error increased by 5%. The additional data point helped

571 decrease the errors for the estimated mass of the more volatile SOA products (Fig. 9)

572 and especially for the 10^2 μg m^{-3} bin. The ΔH_{vap} and α_m estimated values were only

573 slightly affected by the additional measurement.

574   By comparing the results Tests B1 and B2 with Case A, one would expect that

575 the retrieved volatility distribution of the products will be quite similar. The differences

576 present are due to a large extent to the different random experimental errors introduced

577 in the two sets of "measurements" for Experiments A and B. A second reason for the

578 differences is that parametrizations of the two "Experiments" by Pathak et al. (2007b)

579 even if they were derived from the same smog chamber experiments have some

580 differences. As a result, the "true" yields, thermogram, and areogram in Cases A and B

581 are not exactly the same (Figs. 1 and 2).

582   These results suggest that an additional yield measurement at high SOA can

583 lead to a substantial reduction of the error for the estimated yields at low temperatures

584 (Fig. 10) and also a better estimation of the SOA products with higher volatility (10^2

585 and 10^3 μg m^{-3}). These products may contribute little to the SOA concentration at 25

586 ^{o}C, but their reactions (aging) could lead to significant additional SOA in later stages.

587

588 **4.5. Significance of Each Type of Measurement for the Parametrization**

589 To quantify the effect of each type of measurement for the parameter estimation and

590 their subsequent effect on the estimated SOA yields, we repeated tests A1, B1, and C1

591 withholding one set of measurements. More specifically, we used the algorithm

592 providing it the following combination of measurements: TD and isothermal dilution,

593 SOA yields and isothermal dilution, and finally SOA yields and TD.

594   The use of only the TD and isothermal dilution data corresponds for all practical

595 purposes to the previous algorithm of Karnezi et al. (2014) which has been the starting

596 point of this work. In Test A1, the absence of the yield measurements led to a significant

597 deterioration of the ability of the algorithm to estimate SOA yields at all temperatures

598 and concentrations (Fig. S7). The SOA yield error of the algorithm in the 5–35 ^{o}C

599 temperature range increased from 14-24% (when all measurements are provided) to

600 approximately 100% (Table S5). The corresponding uncertainty range also increased

601 by a factor of 4-6 (Table S6). Similar results were obtained in the other tests.

602   Figure S8 shows the volatility distribution of the products, ΔH_{vap} and α_m in Test

603 A1. High discrepancies and uncertainties were observed for the estimated

604 stoichiometric coefficients (α_i), with an increase in the relative error by a factor of 3-4

605 for the 1 and 10 μg m^{-3} bins (Table S7) compared to the case when all three types of

606 measurements are used.

Figures S9 and S10 show the results of the algorithm for Test A1 when only the SOA yields and isothermal dilution measurements are provided as inputs to the algorithm. In this case the algorithm cannot constrain well the ΔH_{vap} (relative error of almost 270% with respect to the true value) as a result of the missing TD measurements. This led to significant increase in the MNE_T for the estimated yields when moving far from the temperature of the measurements (MNE of 65% at 15 ^{o}C and 122% at 5 ^{o}C).

Figures S11 and S12 show the results of the algorithm for Test A1 when only yield and TD measurements are provided as inputs. In this case, there was a significant reduction in the error for the ΔH_{vap} respect to the previous case (from 270% to 50%), but it was still much higher than the 10% error when all three types of measurements were used. This led to better agreement between the true and estimated yields at lower temperatures (MNE_T of 23% and $ARSD$ of 44%).

When comparing TD/Dilution, Yields/Dilution, and Yields/TD results, the Yield/TD combination gave the best results out of the three pairs. The isothermal dilution measurements are the least valuable of the three because only a relatively small fraction of the SOA evaporates and therefore the information provided is relatively limited and focuses on the more volatile components of the particles. Also, TD measurements are important to constrain well ΔH_{vap} and allow the more accurate extrapolation of the results to other temperatures. also provides information for the volatility distribution of the OA. However, our results suggest that the combination of the three types of measurements does need to a major improvement over either the TD/Dilution approach or the Yield/TD approach.

4.6. Sensitivity to the Upper Limit of the Sum of Product Yields
The maximum sum of the VBS product yields is one of the parameters that the user of the algorithm chooses. In the analysis so far, a value of 1 had been selected to reduce the computational cost of the algorithm. Selected tests were repeated using a maximum sum of 2 to quantify the effects of this choice on the estimated parameters and more importantly on the SOA yields predicted by the parameterization. For a 4-product system there are 9,191 product yield combinations and considering the discretization of ΔH_{vap} and α_m, this leads to a total of 367,120 simulations (Table S3).

The increase in the upper limit of the sum of the yields led to an increase in the "good" solutions in Tests A1, A4, B1, B2, and C2. The additional solutions had different yields mostly in the 10^3 μg m^{-3} bin. This led to an increase of the mass yield

of this bin by 37% in Test A1, 47% in Test B1, and 29% in Test C2 (Table S8). The uncertainties were even higher showing once again the difficulty to constrain the IVOC range where there are no SOA measurements at very high SOA concentrations. The new parametrizations had a minor effect on the estimated yields at different temperatures with maximum change in the MNE_T found at 5 $^{\circ}$C (change of 1.8% in Test A1 and 1.2% in Test B2) and much smaller otherwise (Table S9). Therefore, the use of the higher upper limit has an effect on the estimate of the 10^3 μg m^{-3} bin which is quite uncertain in all cases, but has a minor effect on the predicted SOA yields at ambient conditions.

5. Conclusions

An algorithm was developed to estimate VBS parameters for SOA formation combining yield measurements from atmospheric simulation chambers with thermodenuder and isothermal dilution measurements chambers. An additional feature of this approach is that the algorithm estimates the uncertainty of the predicted SOA yields for different SOA concentrations and temperatures, assisting in this way in the design of future experiments.

The algorithm was evaluated against pseudo-experimental data for SOA systems with known properties. The algorithm performed quite well at reproducing the SOA yields at atmospherically relevant concentrations and temperatures with errors less than 20% for practically all cases. This was the case even at temperatures as low as 5 $^{\circ}$C and also when the volatility range used for the parameter estimation was narrower than that of the simulated SOA system. One should note that this error was quite similar in most cases to the experimental error assumed in the construction of the "measurement" datasets.

The errors in the retrieved SOA volatility distributions were in general higher than those of the SOA yields. This is due to a large extent to the existence of multiple solutions that can result in similar yields. The accuracy of the estimated mass fractions of the more volatile SOA components improved when an additional yield measurement at high SOA (e.g., at 200 μg m^{-3}). The addition of this measurement also improved the estimated yields at low temperatures. This therefore suggests that data points at high SOA concentrations should also be obtained experimentally, together with the data points at atmospherically relevant atmospheric SOA levels.

674   In all cases the algorithm results in good estimates of the effective evaporation
675   enthalpy. On the other hand, the estimates of the effective accommodation coefficient
676   are usually quite uncertain. The effect of the mass accommodation coefficient on the
677   measured quantities is relatively small compared to the other parameters (volatility
678   distribution, effective evaporation enthalpy) making it difficult to constrain. This
679   conclusion is consistent with the results of Karnezi et al. (2021). The addition of the
680   SOA yields to the inputs does not make much of a difference, because these are not
681   affected by the accommodation coefficient.

682   The approach combining yield, TD (thermograms), and isothermal dilution
683   (areograms) measurements is recommended for future parametrizations of SOA
684   formation. The use of the results of these experiments that have been designed for the
685   measurement of SOA yields to other applications (e.g., new particle formation) should
686   be performed with caution. Our results indicate that the derived parameterizations are
687   able to predict the SOA yields under different atmospheric conditions with errors of
688   around 20% or less, but the derived volatility distributions can be quite uncertain. These
689   uncertainties are higher for the tails of the distribution (the low volatility and the
690   intermediate volatility organic compounds). Different experiments should be probably
691   performed for the derivation of the VBS distribution if for example on is interested in
692   new particle formation and therefore the low volatility organics focusing on low SOA
693   concentration levels and the least volatile SOA components.

694

695

696   **6. Code and data availability**
697   The   code   and   simulation   results   are   available   upon   request
698   (spyros@chemeng.upatras.gr).

699

700   **7. Supplementary information**
701   The supplement related to this article is available online at: [link]

702

703   **8. Author contribution**
704   PU, and SNP designed the research. PU developed the final model code. AD developed
705   a first version of the code and performed preliminary feasibility tests. DS and SNP
706   designed the experiments for the α-humulene ozonolysis and DS carried them out. PU

performed the simulations, the formal analysis, and wrote the original draft. Paper review and editing was performed by SNP.

9. Competing interests

The authors declare that they have no conflict of interest.

10. Financial support

This work has been supported by the Chemical evolution of gas and particulate-phase organic pollutants in the atmosphere (CHEVOPIN) Project of the Hellenic Foundation for Research and Innovation (HFRI) under grant agreement no. 1819 and the European Union's Horizon 2020 research and innovation program through the EUROCHAMP-2020 Infrastructure Activity under grant agreement no. 730997.

11. References

An, W. J., Pathak, R. K., Lee, B. H. and Pandis, S. N.: Aerosol volatility measurement using an improved thermodenuder: Application to secondary organic aerosol, J. Aerosol Sci., 38, 305–314, doi:10.1016/j.jaerosci.2006.12.002, 2007.

Baltensperger, U., Kalberer, M., Dommen, J., Paulsen, D., Alfarra, M. R., Coe, H., Fisseha, R., Gascho, A., Gysel, M., Nyeki, S., Sax, M., Steinbacher, M., Prevot, A. S. H., Sjögren, S., Weingartner, E. and Zenobi, R.: Secondary organic aerosols from anthropogenic and biogenic precursors, Faraday Discuss., 130, 265–278, doi:10.1039/b417367h, 2005.

Burtscher, H., Baltensperger, U., Bukowiecki, N., Cohn, P., Hüglin, C., Mohr, M., Matter, U., Nyeki, S., Schmatloch, V., Streit, N. and Weingartner, E.: Separation of volatile and non-volatile aerosol fractions by thermodesorption: Instrumental development and applications, J. Aerosol Sci., 32, 427–442, doi:10.1016/S0021-8502(00)00089-6, 2001.

Cain, K. P., Karnezi, E. and Pandis, S. N.: Challenges in determining atmospheric organic aerosol volatility distributions using thermal evaporation techniques, Aerosol Sci. Technol., 54, 941–957, doi:10.1080/02786826.2020.1748172, 2020.

Cappa, C. D.: A model of aerosol evaporation kinetics in a thermodenuder, Atmos. Meas. Tech., 3, 579–592, doi:10.5194/amt-3-579-2010, 2010.

Cappa, C. D. and Jimenez, J. L.: Quantitative estimates of the volatility of ambient organic aerosol, Atmos. Chem. Phys., 10, 5409–5424, doi:10.5194/acp-10-5409-2010, 2010.

Donahue, N. M., Robinson, A. L., Stanier, C. O. and Pandis, S. N.: Coupled partitioning, dilution, and chemical aging of semivolatile organics, Environ. Sci. Technol., 40, 2635–2643, doi:10.1021/es052297c, 2006.

Emery, C., Liu, Z., Russell, A. G., Odman, M. T., Yarwood, G., and Kumar, N.: Recommendations on statistics and benchmarks to assess photochemical model performance, J. Air Waste Manag. Assoc., 67, 582–598, doi:10.1080/10962247.2016.1265027, 2017.

Epstein, S. A., Riipinen, I. and Donahue, N. M.: A semiempirical correlation between enthalpy of vaporization and saturation concentration for organic aerosol, Environ. Sci. Technol., 44, 743–748, doi:10.1021/es902497z, 2010.

Fuchs, N. A. and Sutugin, A. G.: Highly Dispersed Aerosols, Ann Arbor Science Publishers, Ann Arbor, London., 1970.

Fuentes, E. and McFiggans, G.: A modeling approach to evaluate the uncertainty in estimating the evaporation behaviour and volatility of organic aerosols, Atmos. Meas. Tech., 5, 735–757, doi:10.5194/amt-5-735-2012, 2012.

Gao, L., Song, J., Mohr, C., Huang, W., Vallon, M., Jiang, F., Leisner, T., and Saathoff, H.: Kinetics, SOA yields, and chemical composition of secondary organic aerosol from β-caryophyllene ozonolysis with and without nitrogen oxides between 213 and 313 K, Atmos. Chem. Phys., 22, 6001–6020, doi:10.5194/acp-22-6001-2022, 2022

Grieshop, A. P., Miracolo, M. A., Donahue, N. M. and Robinson, A. L.: Constraining the volatility distribution and gas-particle partitioning of combustion aerosols using isothermal dilution and thermodenuder measurements, Environ. Sci. Technol., 43, 4750–4756, doi:10.1021/es8032378, 2009.

Huffman, J. A., Docherty, K. S., Mohr, C., Cubison, M. J., Ulbrich, I. M., Ziemann, P. J., Onasch, T. B. and Jimenez, J. L.: Chemically-resolved volatility measurements of organic aerosol from different sources, Environ. Sci. Technol., 43, 5351–5357, doi:10.1021/es803539d, 2009.

IPCC: Climate Change 2021: The Physical Science Basis. Contribution of Working Group I to the Sixth Assessment Report of the Intergovernmental Panel on Climate

Change, Cambridge University Press, Cambridge, United Kingdom, doi:10.1017/9781009157896, 2021.

Kalberer, M., Paulsen, D., Sax, M., Steinbacher, M., Dommen, J., Prevot, A. S. H., Fisseha, R., Weingartner, E., Frankevich, V., Zenobi, R. and Baltensperger, U.: Identification of polymers as major components of atmospheric organic aerosols, Science, 303, 1659–1662, doi:10.1126/science.1092185, 2004.

Kanakidou, M., Seinfeld, J. H., Pandis, S. N., Barnes, I., Dentener, F. J., Facchini, M. C., Van Dingenen, R., Ervens, B., Nenes, A., Nielsen, C. J., Swietlicki, E., Putaud, J. P., Balkanski, Y., Fuzzi, S., Horth, J., Moortgat, G. K., Winterhalter, R., Myhre, C. E. L., Tsigaridis, K., Vignati, E., Stephanou, E. G. and Wilson, J.: Organic aerosol and global climate modelling: A review, Atmos. Chem. Phys., 5, 1053–1123, doi:10.5194/acp-5-1053-2005, 2005.

Karnezi, E., Riipinen, I. and Pandis, S. N.: Measuring the atmospheric organic aerosol volatility distribution: A theoretical analysis, Atmos. Meas. Tech., 7, 2953–2965, doi:10.5194/amt-7-2953-2014, 2014.

Lane, T. E., Donahue, N. M. and Pandis, S. N.: Effect of NO_x on secondary organic aerosol concentrations, Environ. Sci. Technol., 42, 6022–6027, doi:10.1021/es703225a, 2008.

Lee, B. H., Kostenidou, E., Hildebrandt, L., Riipinen, I., Engelhart, G. J., Mohr, C., Decarlo, P. F., Mihalopoulos, N., Prevot, A. S. H., Baltensperger, U. and Pandis, S. N.: Measurement of the ambient organic aerosol volatility distribution: Application during the Finokalia Aerosol Measurement Experiment (FAME-2008), Atmos. Chem. Phys., 10, 12149–12160, doi:10.5194/acp-10-12149-2010, 2010.

Lee, B. H., Pierce, J. R., Engelhart, G. J. and Pandis, S. N.: Volatility of secondary organic aerosol from the ozonolysis of monoterpenes, Atmos. Environ., 45, 2443–2452, doi:10.1016/j.atmosenv.2011.02.004, 2011.

Lim, S. S., Vos, T., Flaxman, A. D., Danaei, G., Shibuya, K., Adair-Rohani, H., Amann, M., Anderson, H. R., Andrews, K. G., Aryee, M., Atkinson, C., Bacchus, L. J., Bahalim, A. N., Balakrishnan, K., Balmes, J., Barker-Collo, S., Baxter, A., Bell, M. L., Blore, J. D., Blyth, F., Bonner, C., Borges, G., Bourne, R., Boussinesq, M., Brauer, M., Brooks, P., Bruce, N. G., Brunekreef, B., Bryan-Hancock, C., Bucello, C., Buchbinder, R., Bull, F., Burnett, R. T., Byers, T. E., Calabria, B., Carapetis, J., Carnahan, E., Chafe, Z., Charlson, F., Chen, H., Chen, J. S., Cheng, A. T. A., Child, J. C., Cohen, A., Colson, K. E., Cowie, B. C., Darby, S., Darling, S., Davis, A.,

806   Degenhardt, L., Dentener, F., Des Jarlais, D. C., Devries, K., Dherani, M., Ding, E.

807   L., Dorsey, E. R., Driscoll, T., Edmond, K., Ali, S. E., Engell, R. E., Erwin, P. J.,

808   Fahimi, S., Falder, G., Farzadfar, F., Ferrari, A., Finucane, M. M., Flaxman, S.,

809   Fowkes, F. G. R., Freedman, G., Freeman, M. K., Gakidou, E., Ghosh, S.,

810   Giovannucci, E., Gmel, G., Graham, K., Grainger, R., Grant, B., Gunnell, D.,

811   Gutierrez, H. R., Hall, W., Hoek, H. W., Hogan, A., Hosgood, H. D., Hoy, D., Hu,

812   H., Hubbell, B. J., Hutchings, S. J., Ibeanusi, S. E., Jacklyn, G. L., Jasrasaria, R.,

813   Jonas, J. B., Kan, H., Kanis, J. A., Kassebaum, N., Kawakami, N., Khang, Y. H.,

814   Khatibzadeh, S., Khoo, J. P., Kok, C., et al.: A comparative risk assessment of

815   burden of disease and injury attributable to 67 risk factors and risk factor clusters

816   in 21 regions, 1990-2010: A systematic analysis for the Global Burden of Disease

817   Study 2010, Lancet, 380, 2224–2260, doi:10.1016/S0140-6736(12)61766-8, 2012.

818 Louvaris, E. E., Florou, K., Karnezi, E., Papanastasiou, D. K., Gkatzelis, G. I. and

819   Pandis, S. N.: Volatility of source apportioned wintertime organic aerosol in the

820   city of Athens, Atmos. Environ., 158, 138–147, doi:10.1016/j.atmosenv.2017.

821   03.042, 2017a.

822 Louvaris, E. E., Karnezi, E., Kostenidou, E., Kaltsonoudis, C. and Pandis, S. N.:

823   Estimation of the volatility distribution of organic aerosol combining

824   thermodenuder and isothermal dilution measurements, Atmos. Meas. Tech., 10,

825   3909–3918, doi:10.5194/amt-10-3909-2017, 2017b.

826 Odum, J. R., Hoffmann, T., Bowman, F., Collins, D., Flagan, R. C. and Seinfeld, J. H.:

827   Gas/particle partitioning and secondary organic aerosol yields, Environ. Sci.

828   Technol., 30, 2580–2585, doi:10.1021/es950943+, 1996.

829 Pankow, J. F.: An absorption model of gas/particle partitioning of organic compounds

830   in the atmosphere, Atmos. Environ., 28, 185–188, doi:10.1016/1352-

831   2310(94)90093-0, 1994a.

832 Pankow, J. F.: An absorption model of the gas/aerosol partitioning involved in the

833   formation of secondary organic aerosol, Atmos. Environ., 28, 189–193,

834   doi:10.1016/1352-2310(94)90094-9, 1994b.

835 Pathak, R. K., Stanier, C. O., Donahue, N. M. and Pandis, S. N.: Ozonolysis of α-pinene

836   at atmospherically relevant concentrations: Temperature dependence of aerosol

837   mass fractions (yields), J. Geophys. Res., 112, 1–8, doi:10.1029/2006JD007436,

838   2007a.

839 Pathak, R. K., Presto, A. A., Lane, T. E., Stanier, C. O., Donahue, N. M. and Pandis, S.
840   N.: Ozonolysis of α-pinene: Parameterization of secondary organic aerosol mass
841   fraction, Atmos. Chem. Phys., 7, 3811–3821, doi:10.5194/acp-7-3811-2007,
842   2007b.

843 Pope, C. A. and Dockery, D. W.: Health effects of fine particulate air pollution: Lines
844   that connect, J. Air Waste Manag. Assoc., 56, 709–742,
845   doi:10.1080/10473289.2006.10464485, 2006.

846 Quéléver, L. L. J., Kristensen, K., Normann Jensen, L., Rosati, B., Teiwes, R.,
847   Daellenbach, K. R., Peräkylä, O., Roldin, P., Bossi, R., Pedersen, H. B., Glasius,
848   M., Bilde, M., and Ehn, M.: Effect of temperature on the formation of highly
849   oxygenated organic molecules (HOMs) from alpha-pinene ozonolysis, Atmos.
850   Chem. Phys., 19, 7609–7625, doi:10.5194/acp-19-7609-2019, 2019.

851 Riipinen, I., Pierce, J. R., Donahue, N. M. and Pandis, S. N.: Equilibration time scales
852   of organic aerosol inside thermodenuders: Evaporation kinetics versus
853   thermodynamics, Atmos. Environ., 44, 597–607, doi:10.1016/j.atmosenv.
854   2009.11.022, 2010.

855 Saha, P. K. and Grieshop, A. P.: Exploring divergent volatility properties from yield
856   and thermodenuder measurements of secondary organic aerosol from α-pinene
857   ozonolysis, Environ. Sci. Technol., 50, 5740–5749, doi:10.1021/acs.est.6b00303,
858   2016.

859 Seinfeld, J. H. and Pandis, S. N.: Atmospheric Chemistry and Physics: From Air
860   Pollution to Climate Change, Third., John Wiley & Sons, Hoboken, New Jersey.,
861   2016.

862 Sippial, D., Uruci, P., Kostenidou, E. and Pandis, S. N.: Formation of secondary organic
863   aerosol during the dark-ozonolysis of α-humulene, Env. Sci. Atmos., doi:
864   10.1039/d2ea00181k2023.

865 Stanier, C. O., Pathak, R. K. and Pandis, S. N.: Measurements of the volatility of
866   aerosols from α-pinene ozonolysis, Environ. Sci. Technol., 41, 2756–2763,
867   doi:10.1021/es0519280, 2007.

868 Stanier, C. O., Donahue, N. and Pandis, S. N.: Parameterization of secondary organic
869   aerosol mass fractions from smog chamber data, Atmos. Environ., 42, 2276–2299,
870   doi:10.1016/j.atmosenv.2007.12.042, 2008.

871 Stark, H., Yatavelli, R. L. N., Thompson, S. L., Kang, H., Krechmer, J. E., Kimmel, J.
872   R., Palm, B. B., Hu, W., Hayes, P. L., Day, D. A., Campuzano-Jost, P., Canagaratna,

873   M. R., Jayne, J. T., Worsnop, D. R. and Jimenez, J. L.: Impact of thermal
874   decomposition on thermal desorption instruments: Advantage of thermogram
875   analysis for quantifying volatility distributions of organic species, Environ. Sci.
876   Technol., 51, 8491–8500, doi:10.1021/acs.est.7b00160, 2017.

877   Strader, R., Lurmann, F. and Pandis, S. N.: Evaluation of secondary organic aerosol
878   formation in winter, Atmos. Environ., 33, 4849–4863, doi:10.1016/S1352-
879   2310(99)00310-6, 1999.

880   Wehner, B., Philippin, S. and Wiedensohler, A.: Design and calibration of a
881   thermodenuder with an improved heating unit to measure the size-dependent
882   volatile fraction of aerosol particles, J. Aerosol Sci., 33, 1087–1093,
883   doi:10.1016/S0021-8502(02)00056-3, 2002.

884   Zhang, Q., Jimenez, J. L., Canagaratna, M. R., Allan, J. D., Coe, H., Ulbrich, I., Alfarra,
885   M. R., Takami, A., Middlebrook, A. M., Sun, Y. L., Dzepina, K., Dunlea, E.,
886   Docherty, K., DeCarlo, P. F., Salcedo, D., Onasch, T., Jayne, J. T., Miyoshi, T.,
887   Shimono, A., Hatakeyama, S., Takegawa, N., Kondo, Y., Schneider, J., Drewnick,
888   F., Borrmann, S., Weimer, S., Demerjian, K., Williams, P., Bower, K., Bahreini, R.,
889   Cottrell, L., Griffin, R. J., Rautiainen, J., Sun, J. Y., Zhang, Y. M. and Worsnop, D.
890   R.: Ubiquity and dominance of oxygenated species in organic aerosols in
891   anthropogenically-influenced Northern Hemisphere midlatitudes, Geophys. Res.
892   Lett., 34, 1–6, doi:10.1029/2007GL029979, 2007.

893

894

895

Table 1: True and estimated volatility distribution of the products for 8 different tests. The uncertainty of the estimates ($\pm\sigma$) is also included.

TEST	ΔH_{vap} (kJ mol^{-1})	$log(\alpha_m)$	Stoichiometric Coefficients (α_i) at C_i^* (µg m^{-3})						
			10^{-2}	10^{-1}	10^0	10^1	10^2	10^3	10^4
True A	**30**	**-0.30**	**-**	**-**	**0.070**	**0.038**	**0.179**	**0.300**	**-**
A1	32.9±9.6	-0.77±0.47	-	-	0.059 ±0.022	0.071 ±0.052	0.252 ±0.130	0.255 ±0.191	-
A2	32.0±9.8	-0.72±0.45	-	-	0.062 ±0.021	0.067 ±0.053	0.286 ±0.132	-	-
A3	32.0±9.8	-0.72±0.45	-	0.000 ±0.000	0.062 ±0.021	0.067 ±0.053	0.286 ±0.132	-	-
A4	34.0±9.2	-0.70±0.46	-	-	0.062 ±0.021	0.082 ±0.050	0.191 ±0.084	0.259 ±0.198	-
True B	**30**	**-0.30**	**0.001**	**0.012**	**0.037**	**0.088**	**0.099**	**0.250**	**0.800**
B1	33.8±9.2	-0.95±0.21	-	-	0.052 ±0.011	0.037 ±0.039	0.374 ±0.122	0.226 ±0.176	-
B2	36.5±7.6	-0.93±0.26	-	-	0.050 ±0.000	0.051 ±0.039	0.292 ±0.103	0.234 ±0.196	-
True C	**115**	**-2.02**	**0.118**	**0.094**	**0.116**	**0.247**	-	**-**	**-**
C1	104.6±24.0	-1.74±0.97	0.126 ±0.086	0.116 ±0.090	0.154 ±0.116	0.216 ±0.126	-	-	**-**
C2	91.2±19.2	-2.36±0.83	-	-	0.415 ±0.099	0.143 ±0.117	0.137 ±0.113	0.115 ±0.095	**-**

Table 2: The *mean normilized error* (MNE) between the "measurements" and "true" values, and between the "measurements" and the model estimated values for the different tests.

Test	"Measurements" vs "True" [a]			"Measurements" vs Estimated MNE_M [b]		
	Yield	**TD**	**Dilution**	**Yield**	**TD**	**Dilution**
A1	21.2	7.6	9.4	25.0	7.0	16.69
A2	21.2	7.6	9.4	25.1	7.1	16.71
A3	21.2	7.6	9.4	25.1	7.1	16.71
A4	17.8	7.6	9.4	22.4	7.1	19.7
B1	20.5	6.9	5.6	20.6	6.0	14.7
B2	18.1	6.9	5.6	19.1	7.8	18.1
C1	8.4	11.6	1.8	6.3	12.9	3.5
C2	8.4	11.6	1.8	8.6	32.4	2.3

[a] Calculated by $\dfrac{100}{N_O}\sum\limits_{i=1}^{N_O}\dfrac{|O_i - TR_i|}{O_i}$.

[b] Calculated by Eq. (16).

Table 3: The *mean normilized error* between the "true" and estimated values (MNE_T) for the different tests.

Test	Yield				TD	Dilution
	5 ºC	15 ºC	25 ºC	35 ºC		
A1	24.4	21.0	17.3	13.8	5.5	19.0
A2	21.4	19.5	16.9	14.1	4.7	18.5
A3	21.4	19.5	16.9	14.1	4.7	18.5
A4	20.4	18.3	15.7	12.9	6.0	22.5
B1	31.3	21.7	13.9	8.7	4.0	13.3
B2	24.4	15.6	9.0	6.4	2.5	18.4
C1	6.2	6.8	9.6	15.5	4.4 (110 ºC)[*] 10.6 (140 ºC)[*]	2.7
C2	18.1	9.6	7.2	11.5	9.0 (110 ºC)[*] 27.8 (140 ºC)[*]	3.4

[*] The errors for TD were calculated up to the denoted temperature in the parenthesis.

Table 4: The average relative standard deviation (*ARSD*) for the different tests.

Test	Yield				TD	Dilution
	5 ºC	15 ºC	25 ºC	35 ºC		
A1	34.6	29.7	26.0	24.2	21.0	23.6
A2	32.1	28.5	25.2	23.3	21.1	23.2
A3	32.1	28.5	25.2	23.3	21.1	23.2
A4	30.8	27.2	24.5	23.3	21.0	22.1
B1	37.1	27.2	20.0	16.9	20.5	18.0
B2	33.8	25.0	18.5	15.7	18.0	15.9
C1	15.0	14.9	16.2	22.9	20.7[*]	16.5
C2	20.1	15.6	14.1	21.3	20.6[*]	9.8

[*] The *ARSD* for the TD MFR values were calculated in the 20–120 ºC temperature range.
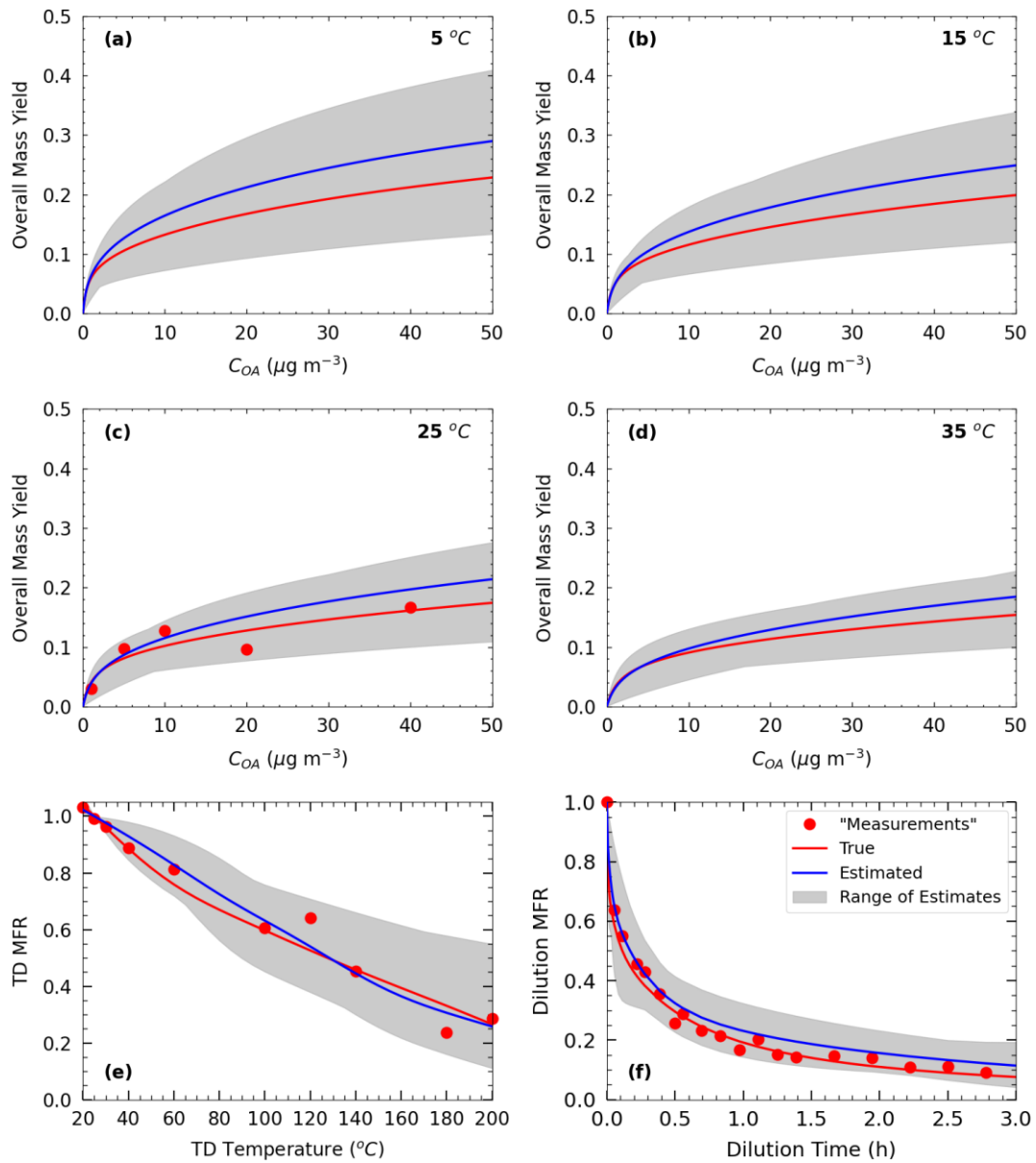
Figure 1: "Measurements" of Test A1 in Experiment A (red dots), true (red line) and estimated (blue line) yields at (**a**) 5 ℃, (**b**) 15 ℃, (**c**) 25 ℃, and (**d**) 35 ℃), (**e**) TD (thermogram), and (**f**) dilution (areogram) values. The grey area shows the range of good solutions obtained by our algorithm.
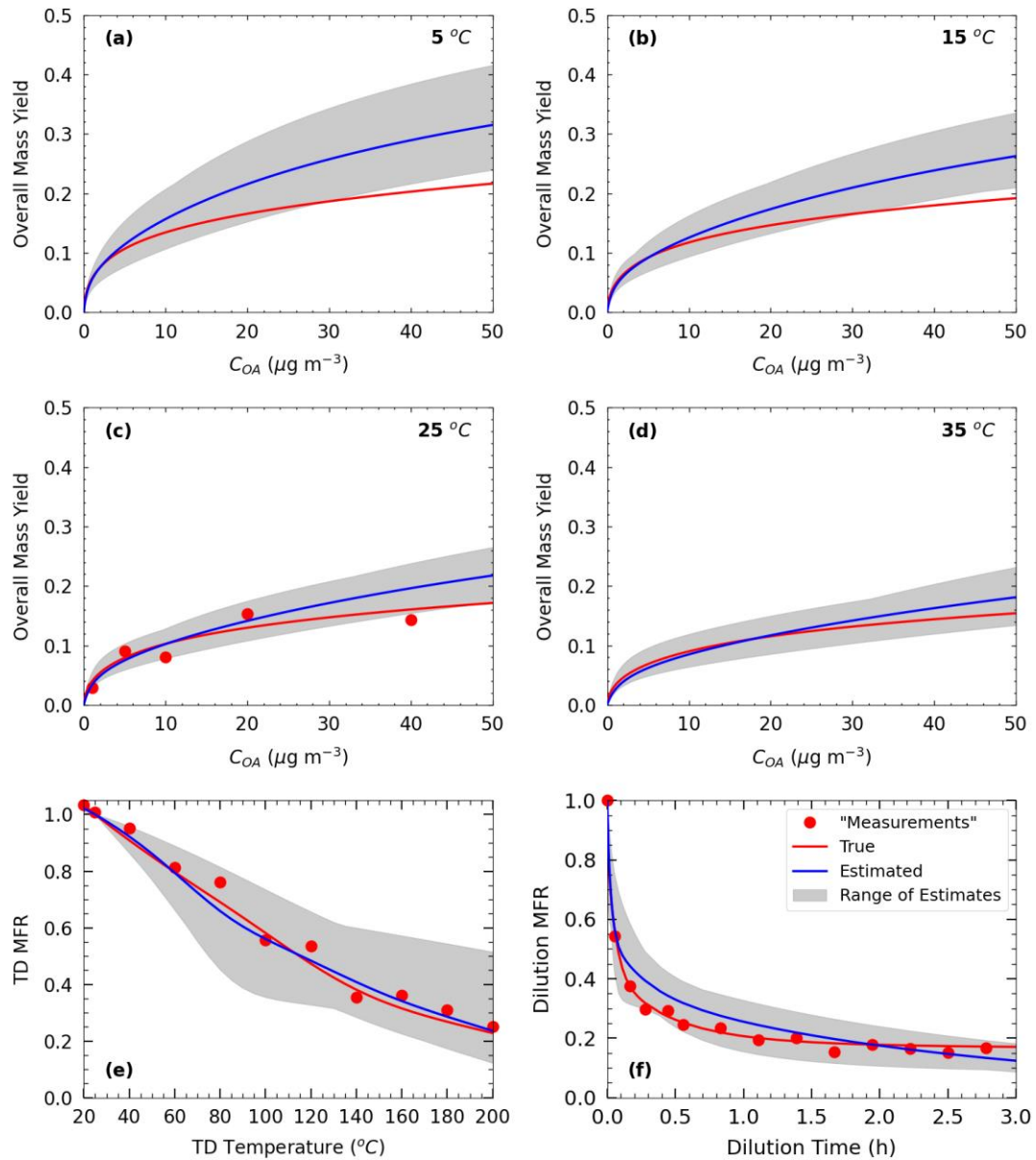
Figure 2: "Measurements" of Test B1 in Experiment B (red dots), true (red line) and estimated (blue line) yields at (**a**) 5 ℃, (**b**) 15 ℃, (**c**) 25 ℃, and (**d**) 35 ℃), (**e**) TD (thermogram), and (**f**) dilution (areogram) values. The grey area shows the range of good solutions.
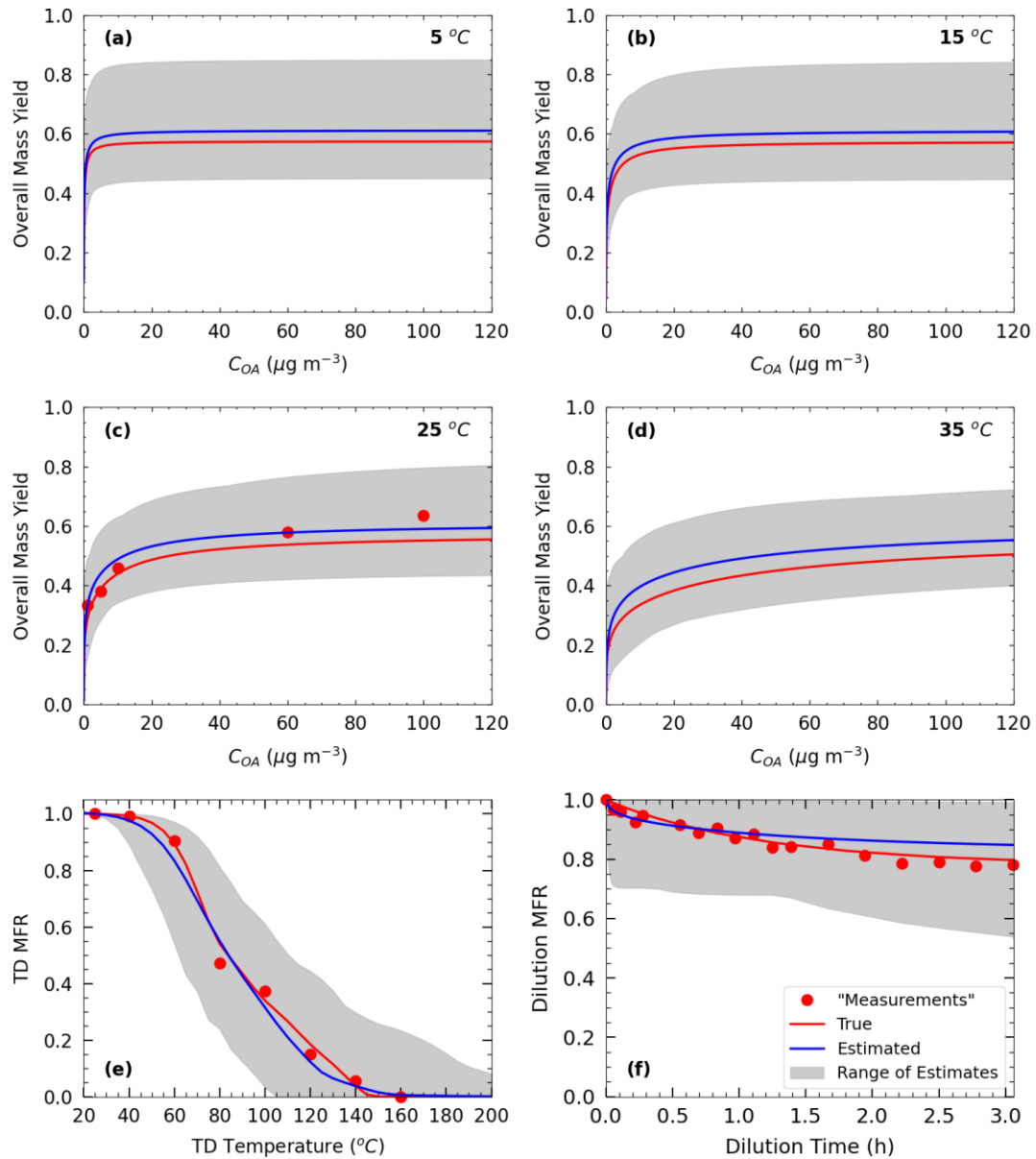
Figure 3: "Measurements" of Test C1 in Experiment C (red dots), true (red line) and estimated (blue line) yields at (**a**) 5 ℃, (**b**) 15 ℃, (**c**) 25 ℃, and (**d**) 35 ℃), (**e**) TD (thermogram), and (f) dilution (areogram) values. The grey area shows the range of good solutions.
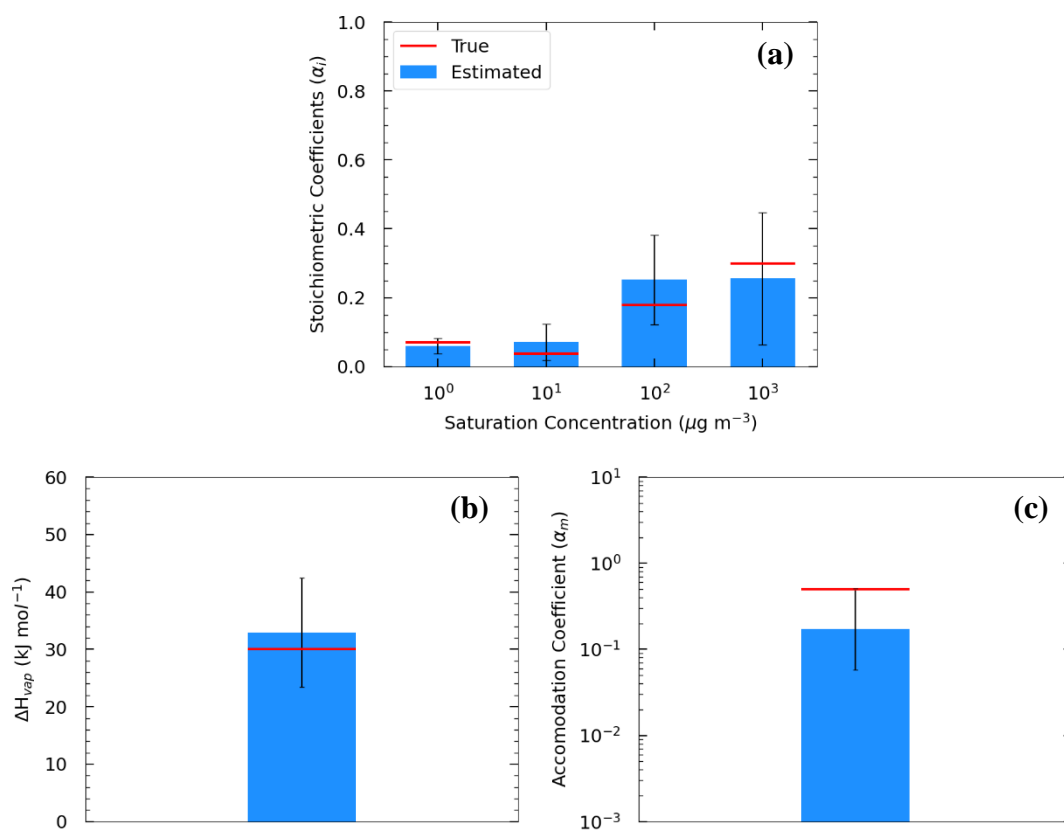
Figure 4. Estimated (bars) and true (red lines) parameter values of Experiment A in Test A1 combining yield, TD, and isothermal dilution measurements for: **(a)** the volatility distribution of the products, **(b)** ΔH_{vap}, and **(c)** α_m. The error bars represent the uncertainty of the estimated values.
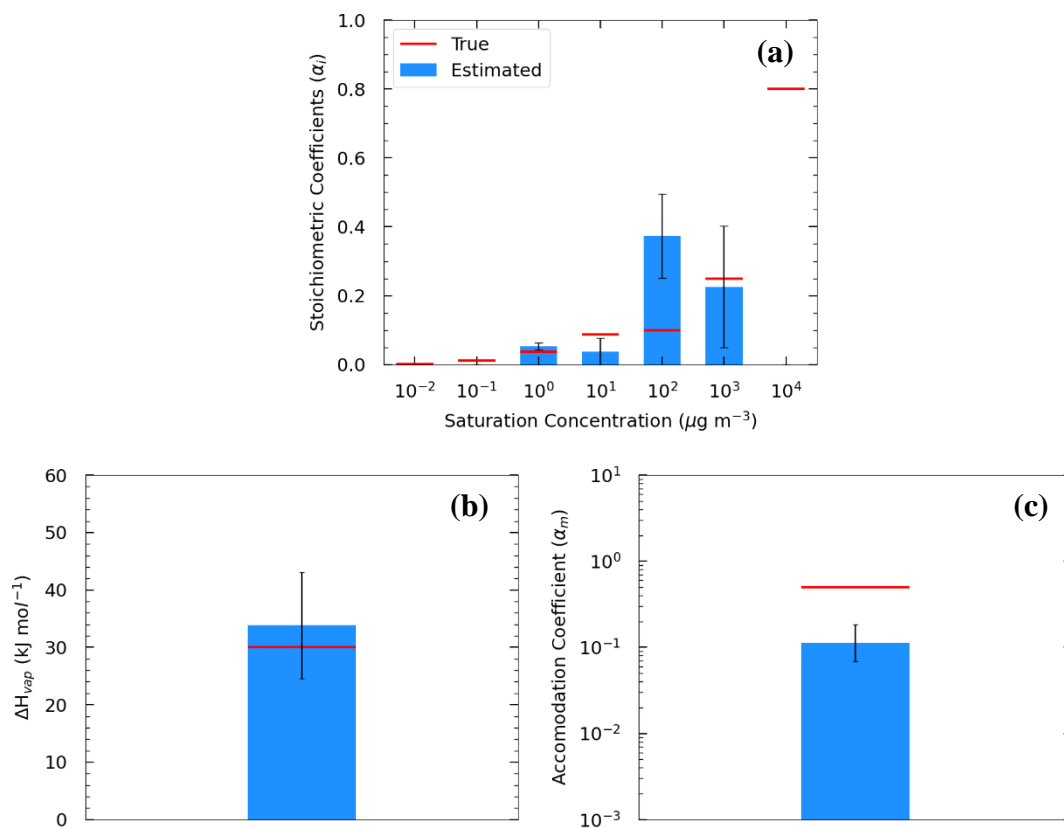
Figure 5: Estimated (bars) and true (red lines) parameter values of Experiment B in Test B1 combining yield, TD, and isothermal dilution measurements for: **(a)** the volatility distribution of the products, **(b)** ΔH_{vap}, and **(c)** α_m. The error bars represent the uncertainty of the estimated values.
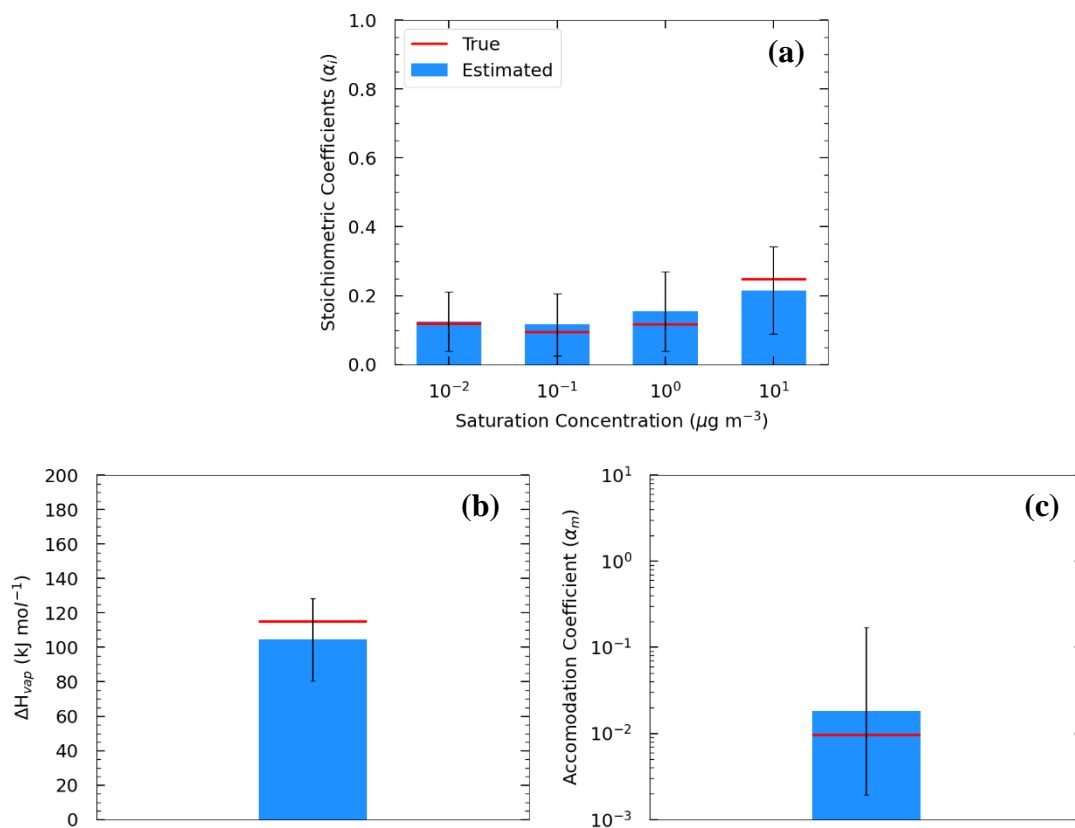
Figure 6: Estimated (bars) and true (red lines) parameter values of Experiment C in Test C1 combining yield, TD, and isothermal dilution measurements for: **(a)** the volatility distribution of the products, **(b)** ΔH_{vap}, and **(c)** α_{m}. The error bars represent the uncertainty of the estimated values.
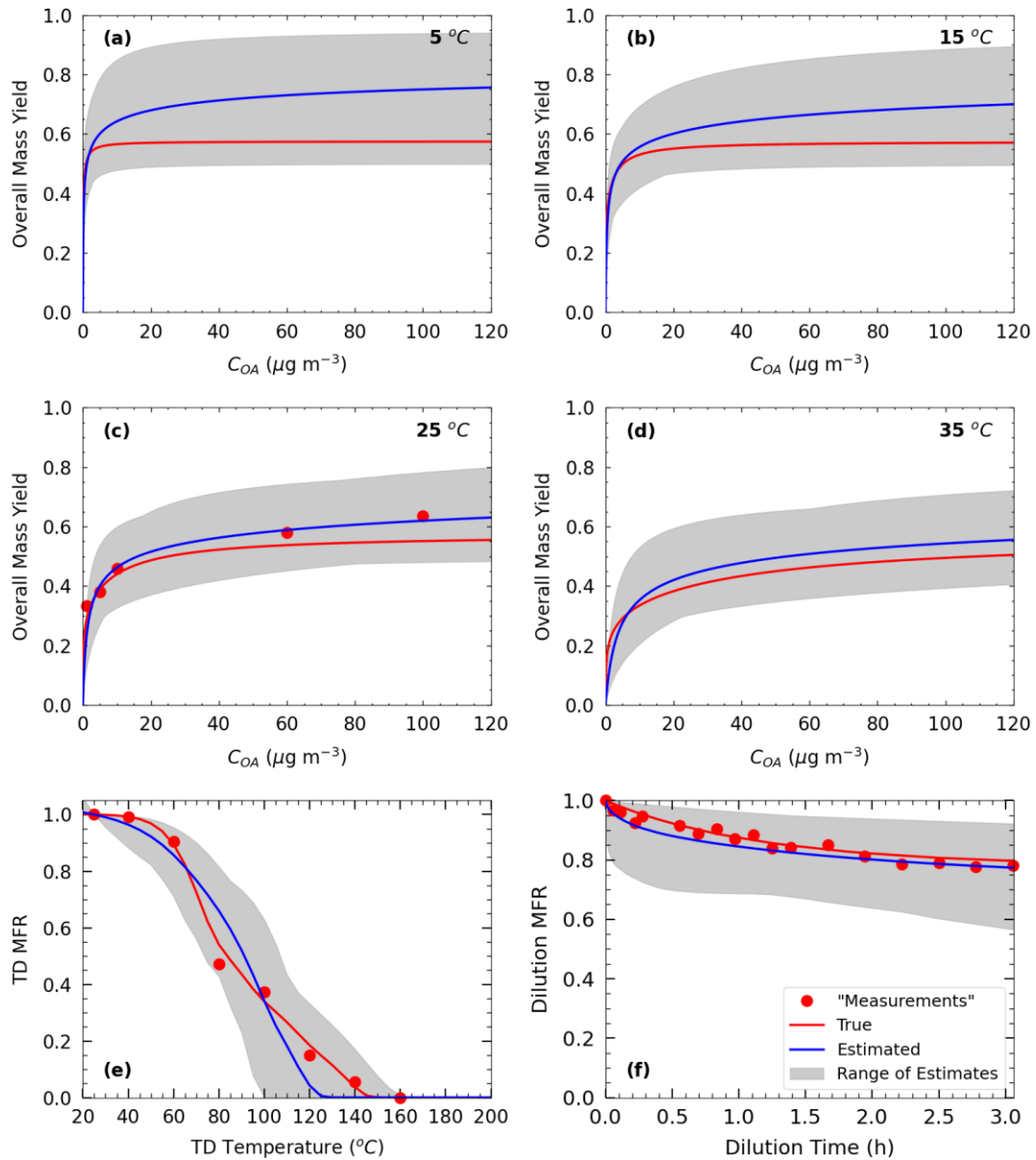
Figure 7: Yields calculated using the "true" parameters of Experiment C (red line) and the estimated (blue line) using the parameters of Test C2 for the following temperatures: (**a**) 5 °C, (**b**) 15 °C, (**c**) 25 °C, and (**d**) 35 °C. Also shown the (**e**) thermogram and (**f**) aerogram. The grey area shows the range of good solutions obtained by our algorithm.
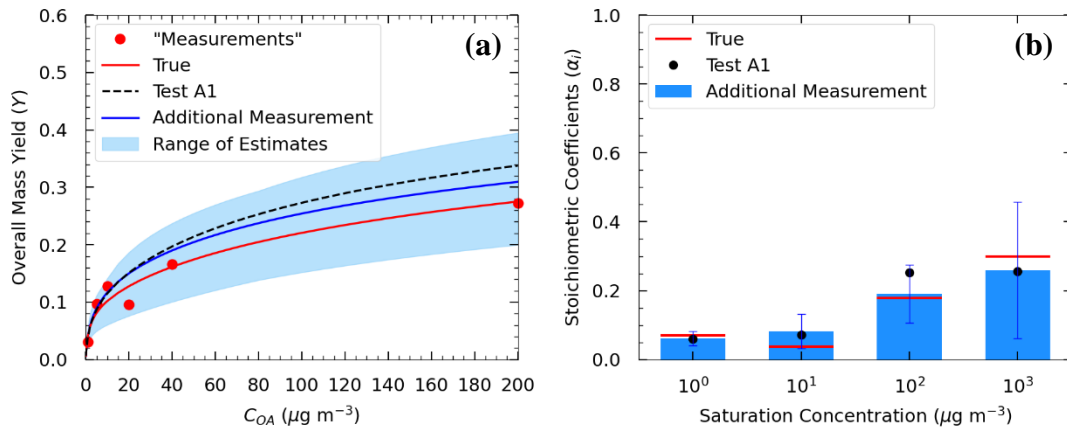
Figure 8: (a) True (red line) and estimated (blue line) yields in Test A4, and the "measurements" of Experiment A (red dots) including an additional yield "measurement" at 200 μg m⁻³. The black dashed line corresponds to the estimated yields in Test A1. **(b)** Estimated volatility distribution of the products (bars) of Test A4 and the true (red lines) parameter values. The black dots correspond to the estimated volatility distribution of the products in Test A1.
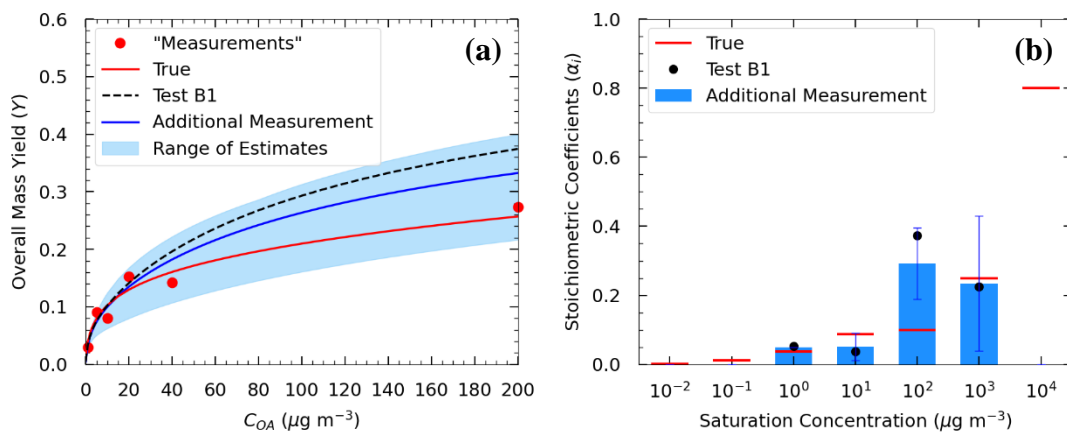
Figure 9: (a) Estimated yields (blue line) in Test B2 and "measurements" of Experiment B (red dots) including an additional yield "measurement" at 200 μg m⁻³. The black dashed line corresponds to the estimated yields in Test B1. **(b)** Estimated volatility distribution of the products (bars) of Test B2 and the true (red lines) parameter values. The black dots correspond to the estimated volatility distribution of the products in Test B1.
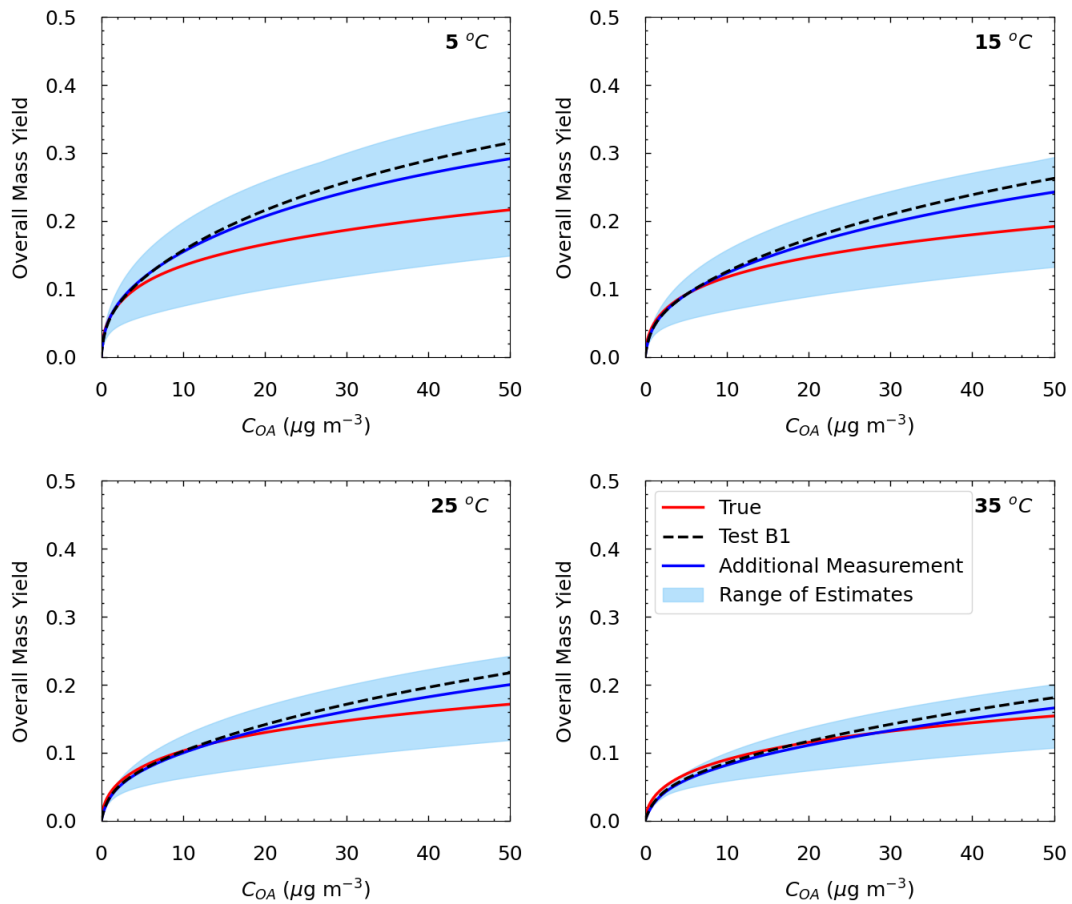
Figure 10: Yields calculated using the "true" parameters of Experiment B (red line) and the estimated (blue line) using the parameters of Test B2 for the following temperatures: 5 ℃, 15 ℃, 25 ℃, and 35 ℃. The blue area shows the range of good solutions obtained by our algorithm. The black dashed line corresponds to the estimated yields in Test B1.